Experimental bifurcation diagram of a solid state laser with optical injection

S. Valling [a,*], B. Krauskopf [b], T. Fordell [a], Å. M. Lindberg [a]

[a] *Accelerator Laboratory, Department of Physical Sciences P.O. Box 64, 00014 University of Helsinki, Finland*

[b] *Department of Engineering Mathematics, University of Bristol, Bristol BS8 1TR, United Kingdom*

Abstract

A method is presented for the automatic construction of an experimental bifurcation diagram of an optically injected solid state laser. From measured time series of laser output intensity, different identifiers of aspects of the dynamics are derived. Combinations of these identifiers are then used to characterize different possible bifurcations. The resulting experimental bifurcation diagram in the plane of injection strength versus detuning includes saddle-node, Hopf, period-doubling and torus bifurcations. It is shown to agree well with a theoretical bifurcation analysis of a corresponding rate equation model.

Key words: Solid state laser; optical injection; nonlinear dynamics; bifurcation diagram
PACS: 42.65.Sf; 42.55.Xi

1 Introduction

Class B lasers are well known to be very sensitive to external influences. Pump modulation, as well as external optical injection and feedback, have widely been reported to cause complex dynamics in this type of lasers, which include semiconductor, solid state and CO_2 lasers; see, for example, [1–3] as entry points to the extensive literature.

* Corresponding author.
Email address: simo.valling@helsinki.fi (S. Valling).

We consider here a laser that receives optical injection of strength K and frequency detuning ω with respect to the free running laser frequency. This system is known for its dynamical complexity, which manifests itself in an intriguing organisation of regions in the (K, ω)-plane corresponding to different laser behaviour. These regions are separated by bifurcation curves, crossings which lead to a qualitative changes of the behaviour, for example, from constant to oscillating laser intensity. The overall arrangement of bifurcation curves is referred to as the bifurcation diagram.

When a mathematical model is present one can find the bifurcation diagram directly from the equations. Good agreement between experiments and a simple rate equation model has been demonstrated both for semiconductor lasers [4] and solid state lasers [5] on the level of stability diagrams in the (K, ω)-plane. Direct numerical integration has been used to map out measures of the dynamics, such as Lyapunov exponents, in the (K, ω)-plane of injected semiconductor lasers [6–8]. Also for injected semiconductor lasers the bifurcation diagram in the (K, ω)-plane has been investigated extensively with the tools of bifurcation analysis [9]. With this approach different types of bifurcations are detected and then followed directly as curves in the (K, ω)-plane; see [10] for an introduction to bifurcation analysis in the context of laser dynamics.

In an experimental setting the bifurcation diagram must be mapped out from experimental data. Due to their internal time scales, experimental observations for semiconductor lasers are mainly based on optical and rf spectra. For CO_2 and solid state lasers, on the other hand, it is possible to obtain sufficiently long and well resolved experimental time series. Experimental stability diagrams have been presented for Fabry-Pérot type semiconductor lasers [11,12], for distributed feedback lasers [4,13] and recently for a Nd:YVO_4 solid state laser [5].

It is important to realise that these bifurcation diagrams were obtained by very different methods. The bifurcation diagrams in [11,4,13] were constructed painstakingly, bifurcation point by bifurcation point, by the experimenter recording a point when a qualitative change was detected in the spectrum according to set criteria. In [14] several spectrum diagrams, where the frequency contents of the laser output was plotted as a function of K, were recorded for different fixed values of ω. The bifurcation diagram was then constructed by the experimenter by determining qualitative changes of the dynamics from this set of spectrum diagrams. Both these methods are quite cumbersome and time consuming. Finally, in [5] a solid state laser was considered and long time series of the laser intensity for slowly increasing K and several fixed values of ω were measured. This information was then plotted in (K, ω)-plane as a colour coding of the intensity of maxima in the time series. While this method is automatic, it leaves the interpretation of the result, that is, the distinction between different dynamics, to the viewer of the resulting image.

In this paper we present a method that allows the automatic construction of an experimental bifurcation diagram in the (K, ω)-plane for an optically injected Nd:YVO_4 solid state laser. By this we mean that regions of different dynamics and bifurcation curves between them are detected automatically. As in [5], we use long time series recordings of the laser intensity for slowly increasing K and several fixed values of ω. We then process this recorded data automatically by identifying different characteristic properties of the (relative) maxima in the time series over a moving observation window. This window must be chosen large enough so that sufficiently many maxima are in it, but sufficiently small to ensure that the time series is quasi-static (does effectively not change with K on the level of the measurement accuracy). This requires very long experimental time series. Furthermore, the noise level limits the reliable detection of (relative) maxima with a small laser intensity. This is reflected in our criteria for the detection of maxima. From the different properties of maxima in the moving observation window we deduce different dynamics and even detect curves of different bifurcation. This works well for saddle-node, Hopf and period-doubling bifurcations. Even torus bifurcations are detected with acceptable accuracy. We demonstrate that the resulting automatic experimental bifurcation diagram agrees well with the bifurcation analysis of a rate equation model.

The paper is organised as follows. In Sec. 2 we discuss how we measure experimental time series and explain how we obtain a time series of maxima. Section 3 explains how we extract information automatically in terms of different indicators. How the indicators can be used to detect bifurcations is discussed in Sec. 4. The resulting automatically detected bifurcation diagram is compared in Sec. 5 with the corresponding theoretical bifurcation diagram. We conclude and point to future work in Sec. 6.

2 Experimental time series data

The experiment consists of two diode-pumped Nd:YVO_4 microchip lasers in a master-slave configuration; a detailed description is given in [5,15]. Both lasers were ensured to operate in single-mode throughout all measurements. The frequency detuning between the lasers is controlled by changing the temperature of the master laser. The level of injection is controlled by an acousto-optic modulator (AOM) between the two lasers.

Each measurement consists of an oscilloscope recording of a long time series of the slave laser's intensity, where the detuning is kept constant while the injection level is increased from zero to a suitably high value (sawtooth sweep). In this way, we record as long a time series as possible with the available data acquisition capacity. Each measurement is about 10 ms long and consists of

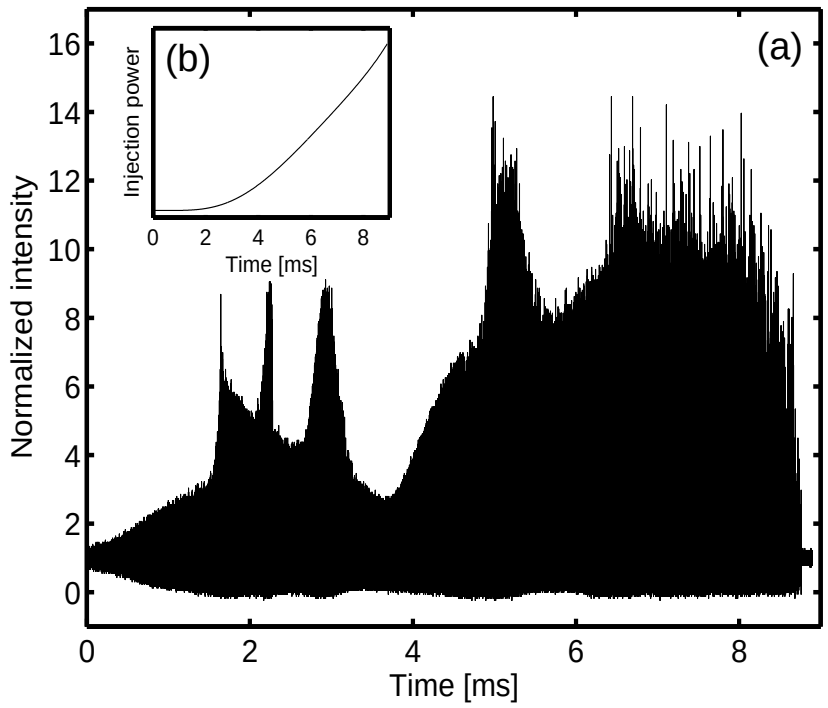

Fig. 1. Time series of normalized laser intensity (a) for a sweep of the injection power (b). The detuning is $\omega \approx -1.0$ and the injection strength K covers the range $[0.0, 1.1]$.

10^6 measurement points. We remark that it is also possible to ramp the injection level back down to zero (triangular sweep), which allows one to observe possible hysteresis loops; see [5]. However, for the work presented here the emphasis is on the best possible measurement resolution.

In each such measurement the detuning was measured directly from the time series of slave laser output intensity. This is possible because for low injection the intensity time series records just the beating between the two lasers. The detuning could also have been measured with a separate detector [5]. The injection power is measured in arbitrary units as a function of time by monitoring the amount of light before it is coupled into the laser. We remark that it is not possible to measure directly the actual injection strength because the coupling constants are unknown; this is a common difficulty in the field and also the case for our setup. For comparisons with the model equations, the measured injection strength was normalized to the quantity K by comparing the experimentally determined lower locking boundary to the numerically determined one; details of this normalization are given in [5].

Many such measurements are performed for a large number of detunings to cover the parameter range of interest. Specifically, and based on earlier studies [5], we consider here the range of $[0.0, 4.0]$ for K and the range $[-4.0, 3.0]$ for

the directly measurable frequency detuning $\omega = (\nu_M - \nu_S)/f_r$ where ν_M and ν_S are the optical frequencies of the master and the slave laser, respectively, and f_r is the (free-running) relaxation oscillation frequency of the slave laser. The time interval between points in the measurements was chosen to be 10 ns, so that at least six points are recorded for each 'basic period' (the period of oscillation of the corresponding frequency detuning) to recognize waveforms correctly. This is because for this system $f_r = 4.3$ MHz and, in the measurement range of $\omega \in [-4, 3]$ the fastest oscillations are about 17 MHz. The point interval of 10 ns and record length of 10^6 points limit the total sweep time to 10 ms. The sweep time could also be limited by the stability of the detuning; in our setup, the fluctuation of detuning within 10 ms is less than 200 kHz, leading to resolution of better than 0.05 for ω. Furthermore, the total sweep time of 10 ms is long enough so that a suitable amount of time series data is recorded for each dynamical state.

A typical measured time series for fixed ω is shown in Fig. 1. The laser output intensity is shown in panel (a); throughout this paper, the laser's intensity is normalized with respect to its free-running value. This means that the intensity of the free-running laser, as well as that in a locked state, is (very close to) 1. The concurrent sweep of the injection power is shown in Fig. 1(b). The time series begins with relaxation oscillations of a solitary laser for zero injection strength and ends up with injection locking for large injection strength. In the example of Fig. 1, $\omega \approx -1.0$ and the maximum of the injection power sweep corresponds to a value of $K \approx 1.1$.

2.1 Identification of maxima

The automatic detection of dynamics and bifurcations is based on criteria concerning relative maxima in the time series. Hence, the first task is the automatic detection of these maxima in a long experimental time series such as that in Fig. 1(a). Our practical definition of a (local) maximum is as follows.

The data point X is a (local) maximum if it is

(a) the largest point of the interval $(X - T/4, X + T/4)$, and
(b) at least I_n larger than either point $X + T/2$ or point $X - T/2$, where T is the basic period.

Here the intensity threshold I_n for the detection of a maximum in (b) represents the noise floor of the system. It is included so that noise does not lead to the detection of maxima that are not due to the underlying laser dynamics. On the other hand, I_n should not be too large because this would prevent the detection of genuine smaller local maxima. We use $I_n = 0.4$.

The above definition is practical and workable in that clearly distinguished peaks of the time series are detected as maxima. While some detail of the dynamics, that is, genuine local maxima, may not be detected (especially between pulses) we found that such detail is beyond what can be detected reliably in experimental data. In fact, different values of I_n and even other definitions of local maxima, did not improve on the results reported here. In particular, our approach is not that critical to noise because it does not rely on the detection of small, possibly random maxima. Similarly, one might try to extract similar and possibly complementary information by detecting (local) minima of the time series. However, the effects of noise are much more severe in the case of minima, and we found that their detection is not practical.

We further distinguish between large and small maxima as follows. A large maximum is defined here as exceeding an amplitude threshold I_m and being larger than its two neighbouring maxima. We found that the value of $I_m = 1.4$ allows us to distinguish genuine, large maxima from small, possibly random maxima. (Recall that the free-running laser intensity is scaled to 1 and, hence, the locked laser output is also very close to 1.) We remark that the maxima of almost sinusoidal oscillations of basic period 1 are identified separately as large maxima. To ensure that all other large pulses in the time series are detected as such, it is necessary to have at least one smaller maximum between them. We therefore introduce an extra maximum in every interval without local (small) maxima that is longer than 1.5 times the basic period. We stress that these extra maxima are only used for the reliable detection of large maxima; they do not appear as detected small maxima.

Figure 2 shows all maxima that have been detected automatically with our method for the time series in Fig. 1. The black dots denote large maxima and the grey dots small maxima. Figure 2(a) presents the whole time series, whereas Fig. 2(b) shows an enlargement (starting from about 6.3 ms) that indicates detected maxima in the original data. As is shown in the following sections, the large maxima that form the upper envelope of the original time series, together with the small maxima, contain the essential information on the dynamics.

3 Indicators for different dynamics

In the data analysis a window of length 5000 points (50μs) was moved over the time series in steps of 1000 points with the aim of determining different identifiers from the maxima of the time series. The observation window length was chosen so that it contains at least a hundred basic periods of the dynamics. With the choice above, the window was short enough to ensure a quasistatic injection strength, that is, practically constant K inside each ob-

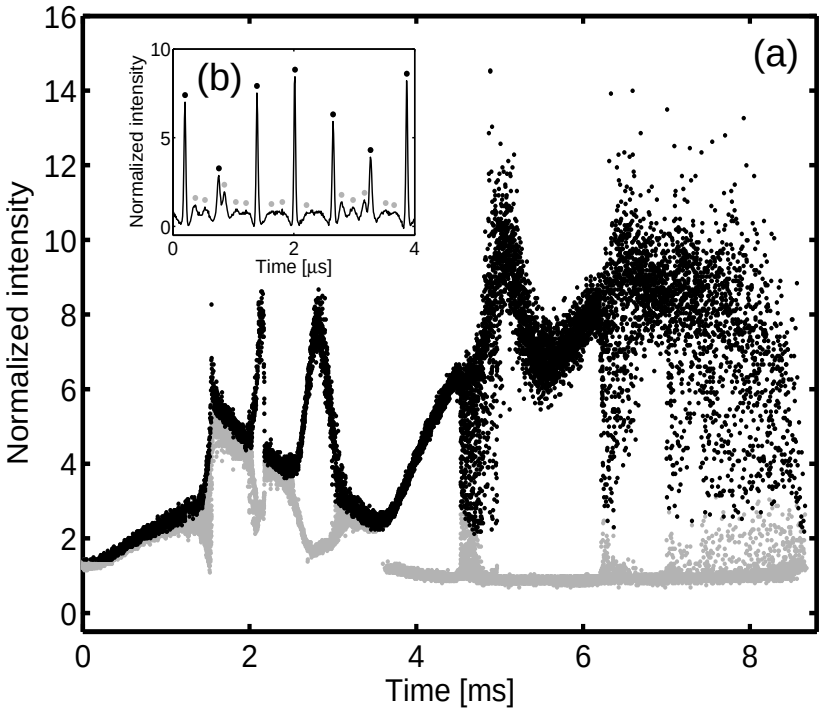

Fig. 2. All the maxima detected from the time series of Fig. 1(a) are marked with dots in panel (a). Those defined also as large maxima are black and the other maxima are grey. Panel (b) shows and enlargement that starts at about 6.3 ms.

servation window. On the other hand, the window was long enough to include a considerable number of oscillations to allow for the reliable identification of the dynamical state in the presence of experimental noise.

In this section we discuss different indicators that are determined automatically from the experimental data. With these indicators different dynamical regimes and even bifurcations can be detected. As a starting point we consider the immediate idea of plotting the size of the largest maximum in each observation window of the (K, ω)-plane. This simple representation of the dynamics was already used in [5] to give an overall but rough picture of the corresponding dynamics. For the data used here the result is shown in Fig. 3. The largest maximum shows whether the time series is pulsed or whether it contains only small amplitude oscillations. However, the representation in Fig. 3 is not an indicator of the dynamics, because it leaves the distinction of different regions to the reader.

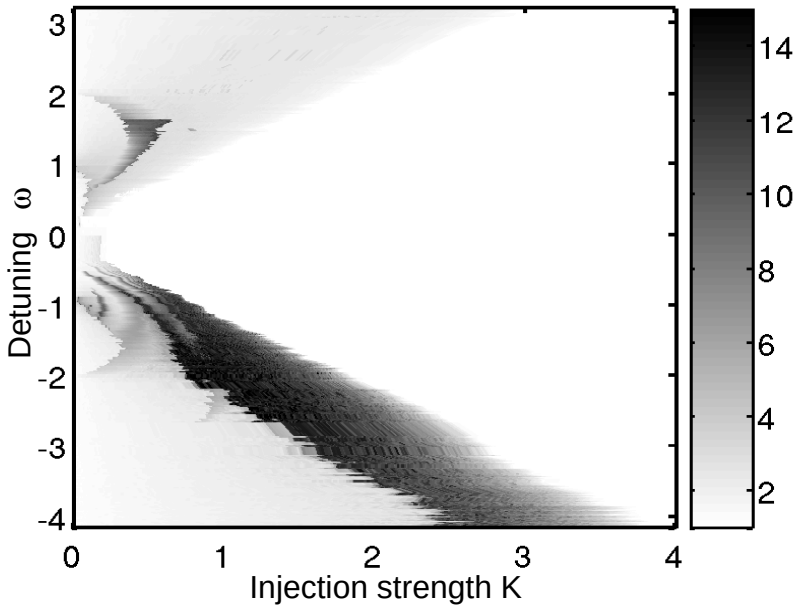

Fig. 3. The intensity of the largest maximum in each observation window as used in [5].

3.1 Detection of periodic orbits

The first indicators that we consider are those for periodic solutions of a given period. Specifically, a period-2 orbit is identified in the series of maxima in a given observation window if at least ten consecutive periods of period two were found. Similarly, a period-3 orbit is identified by at least eight consecutive periods of period three. These choices depend on the measured time series data. If the number of required periods is too small then effects of noise may cause a lot of random counts. Conversely, too strict requirements (long observations) may cause periodic dynamics not to be observed at all.

The detected regions of period-2 oscillations in the (K, ω)-plane are plotted in Fig. 4(a1) and those of period-3 oscillations in Fig. 4(b1). Corresponding typical waveforms are plotted in Figs. 4(a2) and 4(b2), respectively. Indeed, the detected regions give direct information on the dependence of the dynamical state of the system on the two experimental control parameters. The period-2 dynamics is found in two main regions, and there are only very few isolated points due to spurious detection. Two main regions of period-3 dynamics lie to the right of the period-2 regions, which is consistent with the theoretical possibility of windows of period-3 dynamics in a region of chaos beyond successive period-doublings. Further period-3 dynamics is picked up for larger K in the region of negative detuning ω. As we will see below, this is a region with quasiperiodic or locked dynamics on a torus. Hence, the existence of period-3 dynamics is plausible. Overall, Fig. 4(a1) and (b1) demonstrate that the

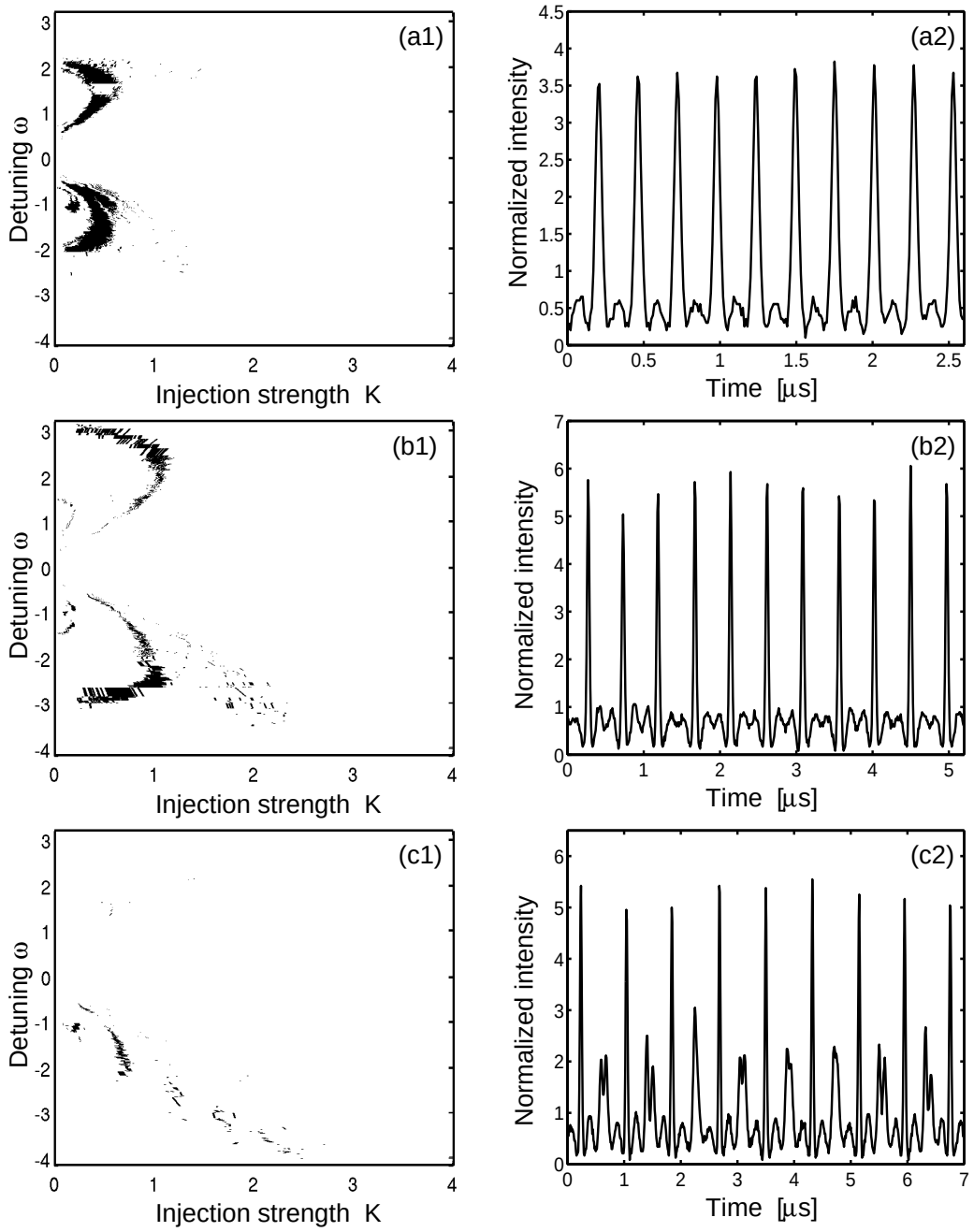

Fig. 4. Identification of regions in the (K, ω)-plane with periodic dynamics of different periods. Panel (a1) shows the period-two regions and panel (a2) is a typical short time series for $(K, \omega) = (0.35, 1.8)$; panel (b1) shows the period-three regions and panel (b2) is a typical short time series for $(K, \omega) = (0.75, -1.3)$; panel (c1) shows the period-four regions where the large maxima have period two and panel (c2) is a typical short time series for $(K, \omega) = (0.55, -1.3)$.

automatic detection works well.

The detection of higher periods is more difficult because some of the maxima

involved may become so small that they are hard to distinguish from the noise floor. To detect period-4 orbits we consider the sequence of largest maxima and determine when this sequence is of period two. The resulting regions in the (K, ω)-plane are plotted in Fig. 4(c1), while Fig. 4(c2) shows a typical waveform. We find period-4 regions past the period-2 regions (as to be expected in the presence of successive period-doublings), as well as for larger K and negative ω, which are the regions of dynamics on a torus.

We remark that the regions of periodic dynamics in Fig. 4 could be separated further, especially in the case of period-3 or period-4, by considering further requirements on amplitude or frequency of the oscillation. For example, the order of large maxima is of topological interest; compare [16] where topological information is derived from short nonstationary time series of a triply resonant optical parametric oscillator.

3.2 Statistical properties of time series

We now introduce four indicators that show certain statistical aspects of the dynamics in the (K, ω)-plane. Apart from being of interest in their own right, we will use combinations of indicators in the next section to detect bifurcation curves, that is, qualitative changes of the dynamics.

Figure 5(a) shows the standard deviation between the maxima in an observation window, which provides an insight into the amplitude distribution of the maxima; compare with Figure 3. This indicator brings out the general regions of dynamics with varying maxima.

It is useful to know if the maxima of an observation window densely fill the range between the largest and smallest amplitude or if there are 'empty intervals' of amplitudes that never occur. As a measure for this, the grey scale of Fig. 5(b) indicates the length of the largest empty interval between maxima (of the time series of maxima). One finds a large value if the maxima inside the observation window are concentrated around some specific levels, as is the case, for example, in Fig. 2 in the range of 5–6 ms. Long largest empty intervals are observed for stable periodic or pulsed states. On the other hand, for stable quasiperiodic or chaotic dynamics we find only very small largest empty intervals, such as in Fig. 2 around 4.5 ms and 8 ms. In other words, the indicator in Fig. 5(b) is very useful to distinguish between pulsed states and quasiperiodic dynamics, which are quite difficult to separate by other means.

The next indicator concerns the characteristic frequency associated with the large maxima. In Fig. 5(c) we show the time averaged interval between large maxima in rounded multiples of the basic period, that is, the period of the corresponding oscillation due to the detuning. This indicator picks up the

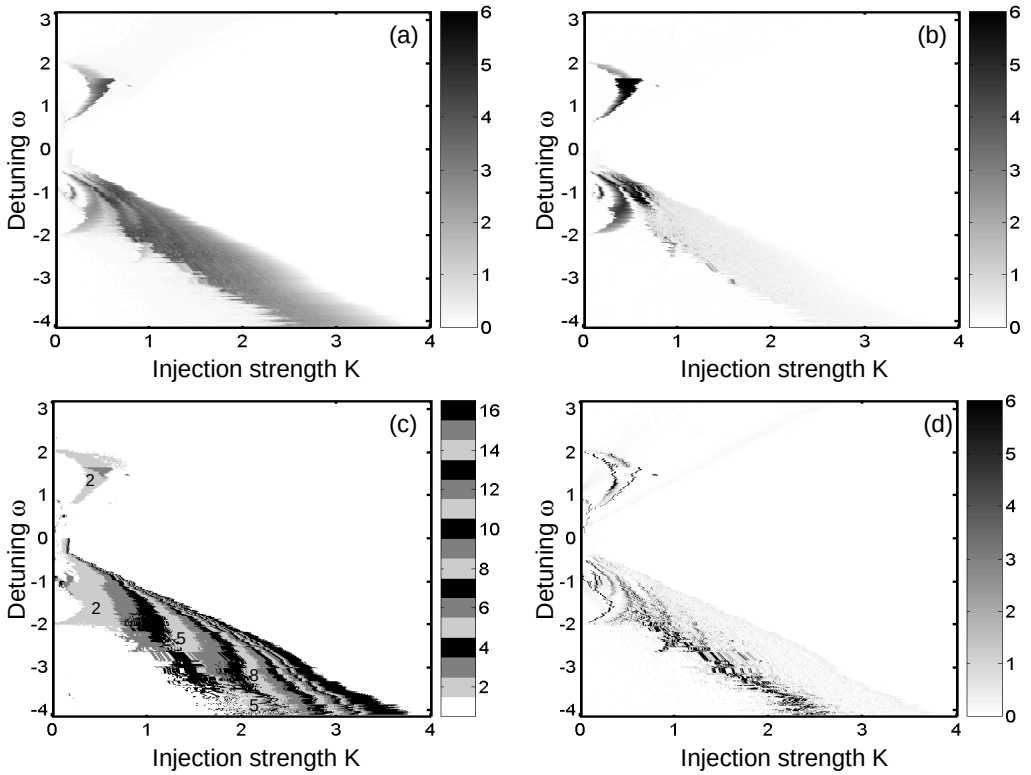

Fig. 5. Indicators used in the identification of bifurcations. Panel (a) shows the standard deviation of maxima in an observation window, and panel (b) shows the largest distance between maxima in an observation window. Panel (c) shows the number of basic periods between large maxima; the numbers in the light grey areas are added to make the periodic grey scale plot clearer. Panel (d) shows the difference between histograms in neighbouring observation windows.

approximate period of the oscillation for all periodic states, including the period-1 oscillations. Notice the region of period-2 orbits in comparison with Fig. 4(a1) and the striped nature of regions with increasing periods. We note that it is convenient to determine this information from the large maxima (and not all maxima), because this immediately gives the period of a periodic state. Furthermore, it is less affected by noise since large maxima are all clearly recognized. Finally, in a pulsed regime, a peak may display two peaks very close to each other; compare Fig. 4(c2). Determining the average frequency only from large maxima (which are isolated by definition) ensures that this does not lead to a spuriously detected very small periods. We found that the average period determined by the large maxima remains quite constant over an observation window, which validates our approach.

The final indicator in Fig. 5(d) is meant to pick up changes between neighbouring observation windows. Specifically we plot a measure of the difference between histograms of all points of neighbouring observation windows. The histogram h of a certain window is constructed by dividing the amplitude

range $[0, 15]$ into 15 subintervals of equal length. We use a continuous definition of the histogram h to avoid the problem that artificial differences between discrete neighbouring histograms might be created due to the arbitrary choice of subintervals. In other words, detected differences are indeed chiefly due to different dynamics. Concretely we determine for each point a weight w for the subinterval h_i it falls into and also assign the weight $(1 - w)$ to the closest neighbouring subinterval, say, h_{i+1}. The weight w is linear and ranges from 1 at the midpoint to 0.5 at the endpoint of a subinterval. We found it useful to calculate the histograms on the basis of all measured points, that is, the original raw data. In this way we avoid a possible sensitivity of this indicator on the exact definition of the maxima. As a measure for the difference d of neighbouring histograms we use

$$d(h, k) = \sum_{i=1}^{15} (h_i - k_i)^2,$$

where h is the histogram of the corresponding observation window and k that of the neighbouring window. The differences are finally divided by the average of all differences to give the indicator a value of reasonable size. Figure 5(d) is colour coded so that dark grey or black means a large difference between the histograms while light grey or white refers to practically identical histograms. While the exact definition of the distance function between histograms is not so important, it influence the choice of thresholds to identify a qualitative change between histograms.

4 Automatic detection of bifurcation curves

The main goal of this paper is the detection of bifurcation curves, which represent qualitative changes of the behaviour of the laser output. Our approach is to specify criteria for each of the possible bifurcations in terms of a suitable combination of indicators as introduced in the previous section. Specifically, we consider saddle-node, Hopf, period-doubling and torus bifurcations. We first discuss each of these bifurcations in turn and then compare the automatically detected bifurcation diagram with its theoretical counterpart.

Saddle-node bifurcation. In a saddle-node bifurcation two equilibria are born, one of which may be stable. In the injected laser system considered here, the bifurcating stable equilibrium corresponds to the locked solution where the laser produces constant output at the frequency of the injected light. In physical terms, the saddle-node bifurcation forms a part of the boundary of the locking region. Crossing it results in a drastic change in the amplitude of oscillation. In addition, due to the pulsing nature of the output, the distribution of maxima has a nonzero deviation before locking. Clearly, after locking this

deviation is practically zero. Therefore, the indicators of the largest maximum and the standard deviation of the maxima are suitable for identifying the saddle-node bifurcation curve. Our practical criterion is the following.

On the locked side of the boundary:

(SN1) the largest maximum is smaller than a (low) threshold value, which depends on the noise level of the system.

On the unlocked side of the boundary:

(SN2) The largest maximum is larger than an upper threshold value;
(SN3) The standard deviation of the maxima is larger than a suitable nonzero threshold value.

For the system considered here we found that lower and upper thresholds for the maxima of 1.3 and 2.0 in (SN1) and (SN2), respectively, work well. The threshold for the standard deviation of the maxima in (SN3) was set to 0.1.

The detected saddle-node bifurcation curve resulting from the above criteria is plotted in Fig. 6(a). The detected saddle-node points form an almost straight line with negative slope in the (K, ω)-plane, which agrees with what is expected [9]. Note that no spurious saddle-node bifurcations are detected.

Hopf bifurcation. At a Hopf bifurcation an equilibrium loses its stability by giving rise to periodic oscillations. It is known that the onset of stable oscillations in a Hopf bifurcation forms part of the boundary of the locking region. To detect it we use the following criterion.

On the locked side of the boundary:

(H1) The largest maximum is smaller than a suitable threshold depending on the noise level.

On the unlocked side of the boundary:

(H2) The largest maximum is larger than that threshold;
(H3) The standard deviation of the maxima is smaller than a suitable threshold value;
(H4) The injection strength is larger than a suitable threshold.

While the criterion for the Hopf bifurcation looks much like that for the saddle-node bifurcation, there is an important difference. The onset of oscillation after a Hopf bifurcation is gradual and not sudden. Specifically, the amplitude of the oscillation grows like a square root with the distance from the bifurcation point [17,18]. Furthermore, the oscillations are initially sinusoidal, which leads to a gradual increase in the deviation of maxima to above its noise level value.

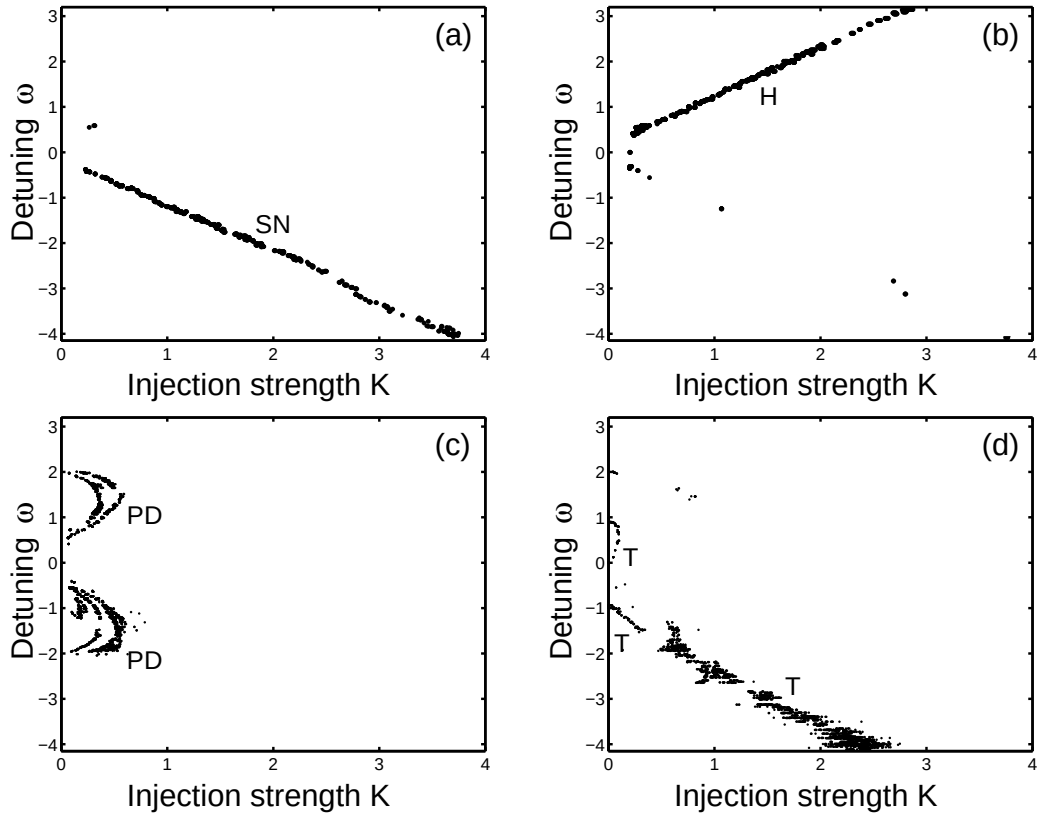

Fig. 6. Experimentally obtained curves of saddle-node (a), Hopf (b), period-doubling (c), and torus (d) bifurcations in (K, ω)-plane.

As a consequence, the threshold values need to be chosen quite carefully.

The Hopf bifurcation curve in Fig. 6(b) was determined with a threshold for maxima in (H1) and (H2) of 1.3 and a threshold for the deviation of maxima in (H3) of 0.1. This detected Hopf bifurcation points lie on an almost straight line with positive slope in the (K, ω)-plane; it forms the other part of the boundary of the locking region [9]. In condition (H4) we used a threshold of 0.2, which ensures that possible spurious solutions for small K are discounted. The problem is that for $K < 0.2$ (where the laser is practically free-running) noise may undamp small relaxation or beating oscillations that may be falsely identified as a Hopf bifurcation. Noise induced oscillations may also occur in parts of the locking region, which is the reson for some spuriously detected Hopf bifurcation points near the saddle-node curve. This effect is only an issue for Hopf bifurcations, since for all other states and bifurcations we are dealing with maxima of considerable size that are definitely above the noise level of the system.

Period-doubling bifurcation. In a period-doubling bifurcation, an attracting periodic orbit loses its stability and gives rise to a new attracting periodic orbit with twice the original period. Here only the first period-doubling curve

is detected so that we consider a change from the basic period to about twice the basic period. We use the following criterion.

(PD1) There is a period-2 sequence in the observation window;
(PD2) The difference of neighbouring histograms is larger than a suitable threshold.

In other words, we are detecting the boundary of the period-two regions detected in Fig. 4(a1). The correct detection of this boundary is achieved by the choice of the threshold for the difference of neighbouring histograms. A good method for determining this threshold is to start from a large threshold value that will reject most points and reducing it until a good representation of the boundary is achieved. To obtain the period-doubling curves in Fig. 6(c), we used the threshold value of 2.0.

Torus bifurcation. In a supercritical torus bifurcation an attracting periodic orbit gives rise to an attracting invariant torus. The dynamics on the torus can be either locked or quasiperiodic. In the locked case there is an attracting periodic orbit on the torus while in the quasiperiodic case, the torus is filled densely. In either case one finds oscillations of a second frequency. However, in the case of locking to low ratios between the two frequencies one finds periodic orbits of low multiples of the basic frequency. Due to the variety of possible time series one may find just beyond a torus bifurcation, the detection of the respective bifurcation curve is quite challenging.

Our approach for identifying torus bifurcation curves is based on the identifier of the largest empty interval between maxima. Indeed the dynamics on the torus tends to fill the amplitude range more densely than the periodic orbit from which it bifurcates. Our criterion is the following.

(T1) The largest empty interval is smaller than a suitable threshold;
(T2) There are no period-2 oscillations in the observation window;
(T3) The interval between large maxima is between a lower threshold and an upper threshold;
(T4) The difference of neighbouring histograms is larger than a suitable threshold.

The threshold for the largest empty interval in (T1) was set to 0.2. Condition (T2) excludes the period-2 oscillations. The condition (T3) allows us to exclude sinusoidal oscillations and oscillations near saddle-node bifurcation curve. While all these also fill the available amplitude range, they do this in a slightly different way. We determined a lower threshold of 2.1 and an upper threshold of 10.0 in (T3) as a good choice. Finally, condition (T4) identifies the boundary of the region with torus dynamics; we used 3.0 as the threshold value. It was derived as for (P2) by starting with very stringent requirements and relaxing them until an acceptable resolution of the torus bifurcations was achieved.

The detected locus of torus bifurcations is plotted in Fig. 6(d). The torus bifurcation curves for small positive and negative detunings are very crisp, whereas the curve for large negative detuning is somewhat blurred. Note that we insist on using the same thresholds throughout, while the dynamics near the curve of torus bifurcations for large negative detunings is actually quite complex.

5 Comparison with theoretical bifurcation diagram

The individually detected bifurcations are assembled in Fig. 7(a) into the overall experimental bifurcation diagram in the (K, ω)-plane. To assess its accuracy, Fig. 7(b) shows the bifurcation diagram of the rate equation model of an injected class B laser [7,19] given by

$$\begin{aligned} \frac{\mathrm{d}a}{\mathrm{d}t} &= [\frac{1}{2}(1-i\alpha)\frac{\gamma_c\gamma_n}{\gamma_s\widetilde{J}}(n-1) - \frac{1}{2}\gamma_p(a^2-1) + i\omega\Omega_r]a + \Omega_r K \qquad (1) \\ \frac{\mathrm{d}n}{\mathrm{d}t} &= \gamma_s(1-n) + \gamma_s\widetilde{J}(1-a^2) + \gamma_n a^2(1-n) + \frac{\gamma_p\gamma_s\widetilde{J}}{\gamma_c}a^2(a^2-1)\,. \end{aligned}$$

Here a and n are the amplitudes of the slowly varying field envelope and the population inversion density, respectively, both normalized to their steady state values. Furthermore, $\widetilde{J} = J/J_{th} - 1$ is the pump rate normalized to its threshold value, α is the linewidth enhancement factor, γ_c is the decay rate of the cavity, γ_s is the decay rate of the upper laser level, γ_n is the relaxation rate of the differential gain, γ_p is the relaxation rate of the nonlinear gain, and Ω_r is the angular relaxation oscillation frequency . The experimentally controllable parameters are the injection strength K and the detuning ω between the master and the slave lasers. Note that noise terms are not included since we are interested in the deterministic bifurcation diagram.

The rate equation model (1) and the procedure to experimentally determine the parameters were introduced in [5]. The operating point of the laser in the measurements of this paper is slightly different, namely given by $\alpha = 0.20$, $\widetilde{J} = 3.3$, $\gamma_c = 2.0 \times 10^{10}\,\mathrm{s}^{-1}$, $\gamma_s = 1.11 \times 10^4\,\mathrm{s}^{-1}$, $\gamma_n = 3.66 \times 10^4\,\mathrm{s}^{-1}$, and $\gamma_p = 0.56 \times 10^6\,\mathrm{s}^{-1}$, which result in a relaxation oscillation frequency of $\Omega_r/(2\pi) = 4.3$ MHz. Note that, in contrast to typical values between 2 and 7 for semiconductor lasers, α is nearly zero for a Nd:YVO_4 laser. The value of $\alpha = 0.20$ was obtained as a combination of fitting [5] and a direct measurement using a FM/AM method [20].

The bifurcation analysis of model (1) was performed with the Matlab package Matcont [21]. The resulting theoretical bifurcation diagram in Fig. 7(b) shows

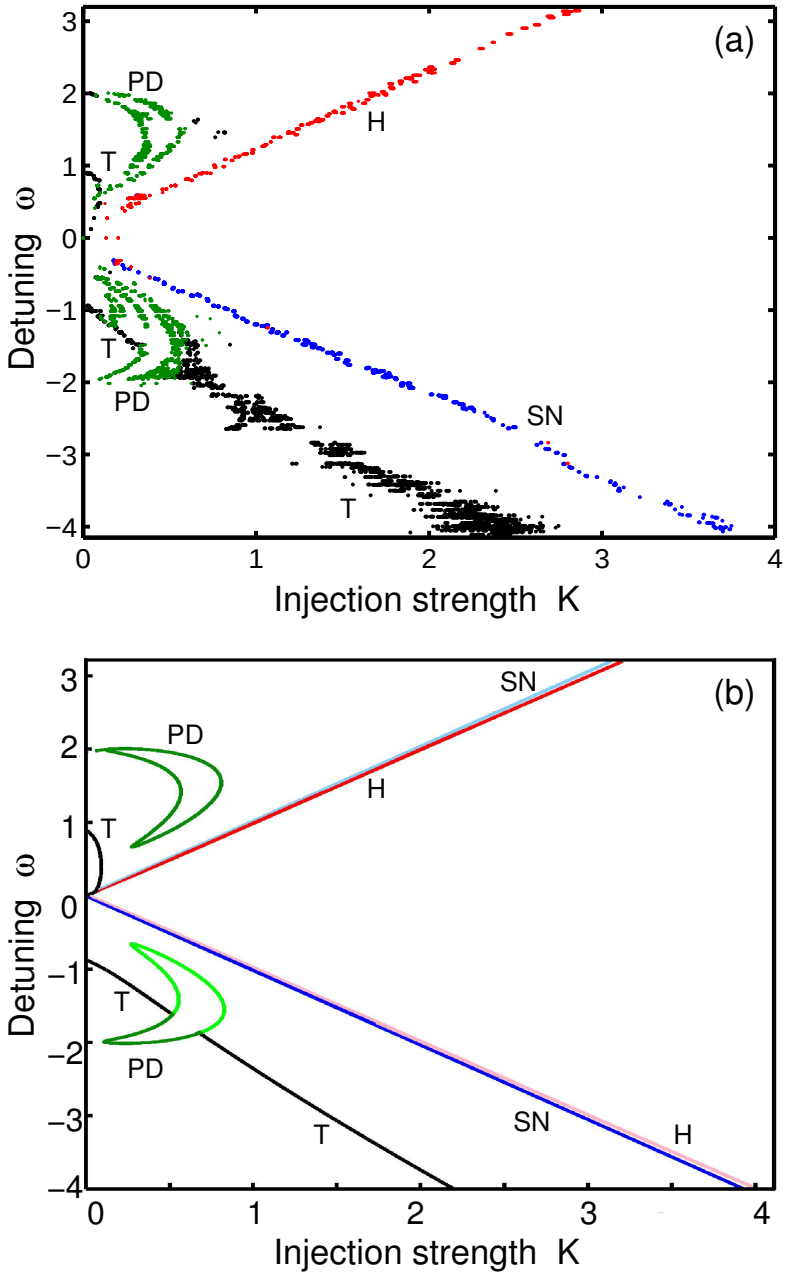

Fig. 7. (Colour online) Bifurcation diagrams showing saddle-node (SN) bifurcations in blue, Hopf (H) bifurcations in red, period-doubling (PD) bifurcations in green, and torus (T)bifurcations in black. Panel (a) is the experimentally obtained bifurcation diagram as collected from Fig. 6(a)-(d). Panel (b) shows the theoretical bifurcation diagram of the rate equation model (1), where bifurcation curves are plotted in dark colour when supercritical and in light colour when subcritical.

the curves of saddle-node, Hopf, period-doubling and torus bifurcations. The bifurcation analysis identifies curves of bifurcations irrespective of the stability of the bifurcating object. In Fig. 7(b) darker curves are of supercritical bifurc-

ations where a stable object bifurcates, while lighter curves are of subcritical bifurcations where an unstable object bifurcates. For a detailed bifurcation analysis of lasers with a small linewidth enhancement factor see [9,22].

The experimental bifurcations of Fig. 7(a) are necessarily all of experimentally observable, that is, stable objects, and they agree very well with the supercritical (darker) bifurcation curves in Fig. 7(b). We stress that the bifurcation diagram of (1) was computed for the experimentally determined parameter values, meaning that no parameter fitting was used. More specifically, the saddle-node and Hopf bifurcation curves in Fig. 7(a) agree extremely well. The period-doublings are also detected where predicted by the rate equations. Interestingly, the subcritical (lighter) part of the lower period-doubling island is detected experimentally. This can be attributed to period-2 dynamics in the time series that appears because it is only weakly damped and excited by noise. There are three separate curves of torus bifurcations in Fig. 7(b), two for negative ω (interrupted by a period-doubling island) and one for positive ω and small K; see also [23] and [22]. All three parts are correctly identified in the experiment. While the detected torus bifurcations for larger negative ω are less well resolved as a curve in the experiment, the detected points nevertheless align reasonably well along the theoretical torus bifurcation curve. We finally remark that the overall agreement between the two bifurcation diagrams in Fig. 7 is as good as that reported for a semiconductor laser in [4]. A key difference is that the experimental diagram presented here was determined automatically.

6 Discussion and conclusions

We presented a method for the automated construction of an experimental bifurcation diagram from time series measurements of an injected Nd:YVO_4 solid state laser. Our approach is to characterize the different bifurcations in terms of indicators that are automatically determined from the experimental data. The characterization of bifurcations is quite generic, but certain threshold values must be set that are system dependent (such as intensity ranges) but also depend on the noise level. However, once the different threshold value have been determined for the system under consideration, they can be used for other measurements. Specifically, we are able to detect saddle-node, Hopf, period-doubling and torus bifurcations. Comparison with a bifurcation diagram of the corresponding rate equations shows excellent agreement for saddle-node, Hopf, period-doubling bifurcations. Torus bifurcations are still detected reliably, but their detected locus is more spread out.

Clearly, our approach works better the cleaner the measured time series data. Certain limitations come directly from the experimental conditions, which

need to strike a balance between the temporal stability of the frequency detuning with the sweep time of the injection power in light of a finite time series data acquisition capacity. Another important consideration is the relative noise level. Already for the quite clean data we used we found difficulties in detecting some pulsation-type periodic orbits, namely when the small maxima between pulses become so small they can not be identified reliably as maxima. For example, there is an empty white area inside the upper period-2 region in Fig. 4(a). This problem can be overcome partly by determining the average time between large maxima in multiples of the basic period. We remark that we were still able to determine the respective period-doubling curve in spite of these difficulties. Noise also somewhat 'blurs' bifurcation curves, which is a well-known effect. This blurring could be kept quite small for saddle-node, Hopf, and period-doubling bifurcations. However, the detected locus of torus bifurcations is quite wide and does not look like a well-defined bifurcation curve. Indeed this bifurcation is the most difficult to detect, even by other means, as it corresponds to the appearance of a second oscillation on top of an existing one. In spite of these difficulties, all relevant curves of torus bifurcations were identified.

The main benefit of the method lies in the automation of the data analysis, as it avoids the painstaking interpretation of the measurements by the experimenter that was required previously to construct mappings of the dynamics. The criteria were chosen as general as possible, so that our method can be applied to other systems as well. First and foremost, one can think of a number of other lasers systems that would allow one to record time series data of similar quality as used here. Natural candidates would be lasers with different kinds of optical feedback or coupled lasers. The essential requirement is that one parameter can be swept controllably in time while the others remain stable enough throughout a sweep. Furthermore, it appears possible to extend the ideas presented here by defining criteria for bifurcations on the basis of spectral data. In this way, automatic bifurcation diagrams could be generated also for semiconductor lasers from data such as the spectral sweeps recorded in [24].

Acknowledgements

Financial support from the Academy of Finland project No. 77582, the Finnish Academy of Science and Letters, Vilho, Yrjö and Kalle Väisälä Foundation, Magnus Ehrnrooth Foundation, Orion Research Fund, Svenska Kulturfonden and Finska Vetenskaps-societen is acknowledged. The work of B.K. was supported by an Engineering and Physical Sciences Research Council (EPSRC) Advanced Research Fellowship grant.

References

[1] G. H. M. van Tartwijk, G. P. Agrawal, Laser instabilities: a modern perspective, Prog. Quant. Electron. 22 (1988) 43.

[2] B. Krauskopf, D. Lenstra (Eds.), Fundamental Issues of Nonlinear Laser Dynamics, Vol. 548 of AIP Conference Proceedings, American Institute of Physics, 2000.

[3] D. M. Kane, K. A. Shore (Eds.), Unlocking Dynamical Diversity: Optical Feedback Effects on Semiconductor Lasers, Wiley, 2005.

[4] S. Wieczorek, T. B. Simpson, B. Krauskopf, D. Lenstra, Global quantitative predictions of complex laser dynamics, Phys. Rev. E 65 (2002) 045207(R).

[5] S. Valling, T. Fordell, Å. M. Lindberg, Maps of the dynamics of an optically injected solid-state laser, Phys. Rev. A 72 (2005) 033810.

[6] K. E. Chlouverakis, M. J. Adams, Stability maps of injection-locked laser diodes using the largest lyapunov exponent, Opt. Commun. 216 (2003) 405.

[7] T. Fordell, Å. M. Lindberg, Numerical stability maps of an optically injected semiconductor laser, Opt. Commun. 242 (2004) 613.

[8] S. K. Hwang, J. M. Liu, Dynamical characteristics of an optically injected semiconductor laser, Opt. Commun. 183 (2000) 195.

[9] S. Wieczorek, B. Krauskopf, T. B. Simpson, D. Lenstra, The dynamical complexity of optically injected semiconductor lasers, Physics Reports 416 (2005) 1.

[10] B. Krauskopf, Bifurcation analysis of laser systems, in: Fundamental Issues of Nonlinear Laser Dynamics, Vol. AIP Conference Proceedings 548, American Institute of Physics, 2000, p. 1.

[11] T. B. Simpson, J. M. Liu, K. F. Huang, K. Tai, Nonlinear dynamics induced by external optical injection in semiconductor lasers, J. Opt. B: Quantum Semiclass. Opt. 9 (1997) 765.

[12] S. Eriksson, Dependence of the experimental stability diagram of an optically injected semiconductor laser on the laser current, Opt. Commun. 210 (2002) 343.

[13] T. B. Simpson, Mapping the nonlinear dynamics of a distributed feedback semiconductor laser subject to external optical injection, Opt. Commun. 215 (2003) 135.

[14] S. Eriksson, Å. M. Lindberg, Observations on the dynamics of semiconductor lasers subjected to external optical injection, J. Opt. B: Quantum Semiclass. Opt. 4 (2002) 149.

[15] S. Valling, T. Fordell, Å. M. Lindberg, Experimental and numerical intensity time series of an optically injected solid state laser, Opt. Commun. 254 (2005) 282.

[16] A. Amon, M. Lefranc, Topological signature of deterministic chaos in short nonstationary signals from an optical parametric oscillator, Phys. Rev. Lett. 92 (2004) 094101.

[17] Yu. A. Kuznetsov, Elements of Applied Bifurcation Theory, Springer-Verlag, 1995.

[18] S. H. Strogatz, Nonlinear dynamics and chaos, Addison-Wesley, 1996.

[19] T. B. Simpson, J. M. Liu, A. Gavrielides, V. Kovanis, P. M. Alsing, Period-doubling route to chaos in a semiconductor laser subject to optical injection, Appl. Phys. Lett. 64 (1994) 3539.

[20] T. Fordell, S. Valling, Å. M. Lindberg, Modulation and the linewidth enhancement factor of a diode-pumped Nd:YVO_4 laser, Opt. Lett. 30 (2005) 3036.

[21] A. Dhooge, W. Govaerts, Yu. A. Kuznetsov, Matcont: A matlab package for numerical bifurcation analysis of odes, ACM Transactions on Mathematical Software 29 (2003) 141.

[22] B. Krauskopf, S. Wieczorek, Accumulating regions of winding periodic orbits in optically driven lasers, Physica D 173 (2002) 97.

[23] M. Nizette, T. Erneux, A. Gavrielides, V. Kovanis, Injection-locked semiconductor laser dynamics from large to small detunings, Proceedings of SPIE 3625 (1999) 679.

[24] S. Eriksson, Å. M. Lindberg, Periodic oscillation within the chaotic region in a semiconductor laser subjected to external optical injection, Opt. Lett. 26 (2001) 142.